ACS APPLIED MATERIALS & INTERFACES

Research Article

Cite This: ACS Appl. Mater. Interfaces 2018, 10, 39809−39818

www.acsami.org

Cobalt-Iron Oxide Nanoarrays Supported on Carbon Fiber Paper with High Stability for Electrochemical Oxygen Evolution at Large Current Densities

Zhiguo Ye,*[,†] Chunlin Qin,[†] Guang Ma,[‡] Xinyuan Peng,[†] Tao Li,[†] Duosheng Li,[†] and Zhong Jin*[,§]

[†]School of Material Science and Engineering, Nanchang Hangkong University, Nanchang 330063, China

[‡]Global Energy Interconnection Research Institute Co., Ltd., Beijing 102209, China

[§]Key Laboratory of Mesoscopic Chemistry of MOE, School of Chemistry and Chemical Engineering, Nanjing University, Nanjing, Jiangsu 210023, China

Supporting Information

ABSTRACT: Here, we demonstrate that nonprecious CoFe-based oxide nanoarrays exhibit excellent electrocatalytic activity and superior stability for electrochemical oxygen evolution reaction (OER) at large current densities (>500 mA cm^{-2}). Carbon fiber paper (CFP) with three-dimensional macroporous structure, excellent corrosion resistance, and high electrical properties is used as the support material to prevent surface passivation during the long-term process of OER. Through a facile method of hydrothermal synthesis and thermal treatment, vertically aligned arrays of spinel $Co_xFe_{3-x}O_4$ nanostructures are homogeneously grown on CFP. The morphology and the Fe-doping content of the CoFe oxide nanoarrays can be controlled by the Fe^{3+} concentration in the precursor solution. The arrays of CoFe oxide nanosheets (NSs) grown on CFP ($Co_{2.3}Fe_{0.7}O_4$-NSs/CFP) deliver lower Tafel slope (34.3 mV dec^{-1}) than CoFe oxide nanowire (NW) arrays grown on CFP ($Co_{2.7}Fe_{0.3}O_4$-NWs/CFP) in alkaline solution, owing to higher Fe-doping content and larger effective specific surface area. The $Co_{2.3}Fe_{0.7}O_4$-NSs/CFP electrode exhibits excellent stability for OER at large current densities in alkaline solution. Moreover, the morphology and structure of CoFeO nanoarrays are well preserved after long-term testing, indicating the high stability for OER.

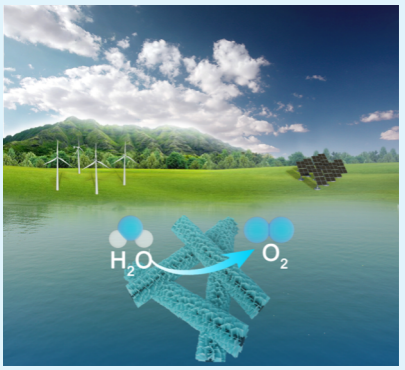

KEYWORDS: *water splitting, cobalt-iron oxide, nanoarray, oxygen evolution reaction, stability*

1. INTRODUCTION

With the rapid increase of distributed power-generation technologies such as wind and solar power plants, the storage of massive excess electricity derived from these intermittent energies is becoming a prominent problem. Electrochemical water splitting for the renewable hydrogen production from these intermittent energies is considered as one of the most promising methods to solve this problem.[1−6] However, the efficiency of energy transformation of electrochemical water splitting for hydrogen production is seriously determined by the sluggish kinetics and the high oxygen evolution reaction (OER) overpotential (η). IrO_2 and RuO_2 with excellent electrocatalytic properties and superior stability are usually employed as electrocatalysts for OER anode, but their scarcity and high cost impede the large-scale industrial application of hydrogen production.[7−11] To overcome these obstacles, it is very crucial to design novel OER catalysts with superior electrocatalytic activity, low cost, environment friendliness, and superior stability for the industrial applications of electrochemical water splitting under large current densities (>500 mA cm^{-2}).

To date, various transition-metal oxides and hydroxides, especially Ni-, Co-, Fe-, and Mn-containing OER catalysts, have been seen as the possible substitutes of precious metal-based OER electrodes, owing to their rich source, low cost, no pollution, and excellent electrochemical stability.[12−18] Among these metal oxides, spinel Co_3O_4 is regarded as one of the most attractive OER catalysts with intriguing advantages of cost-effectiveness, high thermal stability, rich sources, and environment friendliness.[19−23] However, compared to precious RuO_2- and IrO_2-based catalysts, Co_3O_4-based electrode still has poor electrocatalytic activity and high overpotential due to the low amount of active sites and poor conductivity and thus its application for electrochemical water splitting at large current densities is still not practical.[19−23] To improve the electrocatalytic activity at large current densities, the reactivity and the number of active sites need to be further enhanced. So far, two effective strategies have been developed for this purpose. On the one hand, the incorporation of other elements (e.g., Fe, Ni, Mn, etc.) into pristine metal oxides or hydroxides has been proven to efficiently increase the electrocatalytic activity and reduce the overpotential of OER, due to a variation of oxygen

Received: September 4, 2018
Accepted: October 26, 2018
Published: October 26, 2018

DOI: 10.1021/acsami.8b15357
ACS Appl. Mater. Interfaces 2018, 10, 39809−39818

Scheme 1. Schematic Fabrication Process of the $Co_xFe_{3-x}O_4$-NWs/CFP and $Co_xFe_{3-x}O_4$-NSs/CFP Composite Electrodes

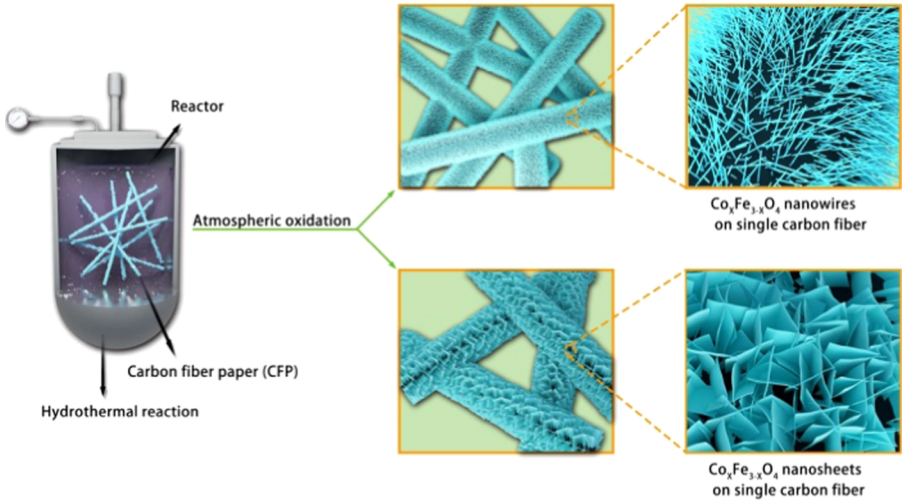

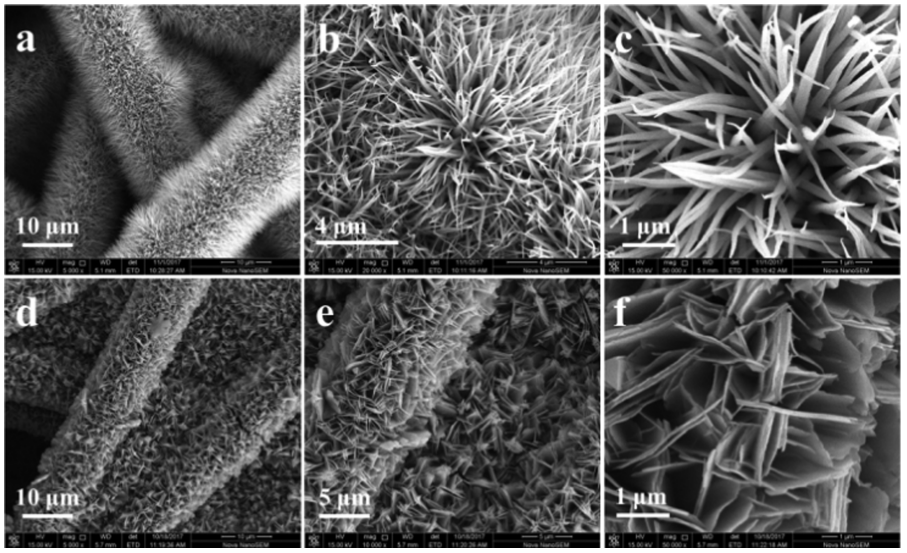

Figure 1. Field emission scanning electron microscopy (FESEM) images showing the morphologies of the $Co_{2.7}Fe_{0.3}O_4$-NWs/CFP (a–c) and $Co_{2.3}Fe_{0.7}O_4$-NSs/CFP (d–f) with different magnifications.

vacancies or a decrease of surface adsorption energy of the intermediate products.[1,18,24−32] For instance, Trotochaud group has confirmed that the Fe addition in Ni oxide can bring a >30-fold increase of conductivity and a great decrease of OER overpotential.[24] In our recent study, it was proved that the doping of other elements in clean metal oxides can increase both the conductivity and electrocatalytic activity of OER catalysts, deriving from the increase of defects or oxygen vacancies in the structures.[18] On the other hand, the structural engineering and nanocrystallization of the electrocatalyst materials could undoubtedly enhance the OER performance. For example, Co_3O_4 nanosheets (NSs), Fe-based nanotubes, Ni-based oxide nanosheets, and so on have been fabricated and demonstrated excellent electrocatalytic activities as OER electrodes.[3,12,20,25,33]

The poor stability of nonprecious metal-based oxide electrocatalysts during OER process, especially at large current densities, is one of the most challenging issues that hinder the massive applications. The IrO_2- and RuO_2-based electrode materials usually have high stability in acidic or neutral solutions. For example, IrO_2/Ta_2O_5 and IrO_2/MnO_2 composites coated on Ti substrate can exhibit superior stability (>800 h) for OER at 2000 mA cm^{-2} in acid solution.[11,34−36] However, the stability evaluation of the present nonprecious metal-based electrodes was usually carried out at <200 mA cm^{-2} with a short period in alkaline media, which is insufficient for the practical stability assessment. Although the electrocatalytic activity of nonprecious metal oxides has been proved to be comparable to that of noble-metal oxides, more efforts should be made to further improve the stability of nonprecious metal-based electrocatalysts.

Here, we demonstrate that both the electrocatalytic activity and OER stability of Co-based oxide electrocatalyst can be greatly enhanced by the incorporation of Fe atoms. Through a facile hydrothermal synthesis and thermal treatment approach, highly homogeneous $Co_xFe_{3-x}O_4$ nanoarrays were grown on carbon fiber paper (CFP) support with three-dimensional macroporous structure, excellent electrical properties, and good electrochemical stability. Benefitted from the excellent electrochemical stability of the $Co_xFe_{3-x}O_4$ nanoarrays, the high passivation resistance of CFP support, and the good interface connect between $Co_xFe_{3-x}O_4$ nanoarrays and CFP

DOI: 10.1021/acsami.8b15357
ACS Appl. Mater. Interfaces 2018, 10, 39809−39818

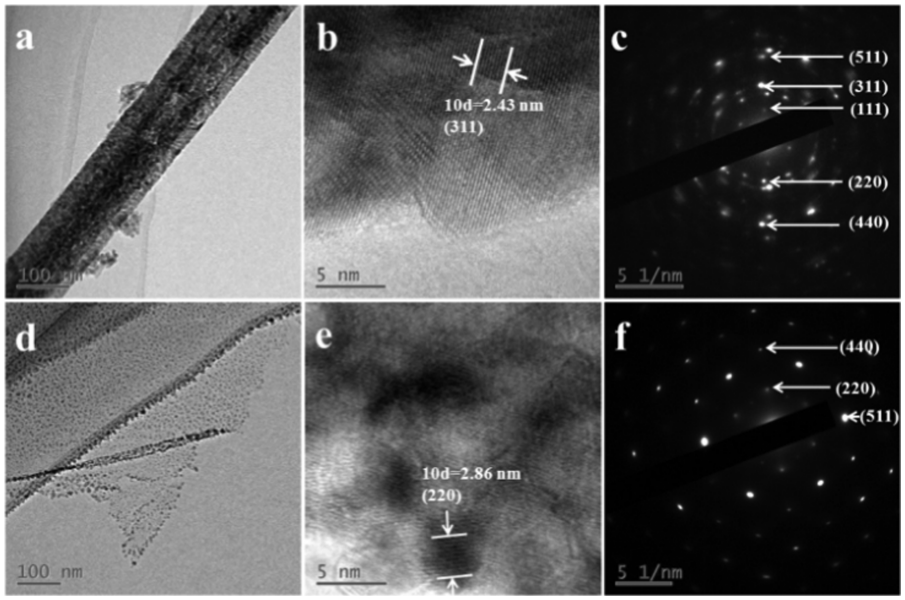

Figure 2. (a) Transmission electron microscopy (TEM), (b) HRTEM, and (c) SAED images of $Co_{2.7}Fe_{0.3}O_4$-NWs/CFP. (d) TEM, (e) HRTEM, and (f) SAED images of $Co_{2.3}Fe_{0.7}O_4$-NSs/CFP.

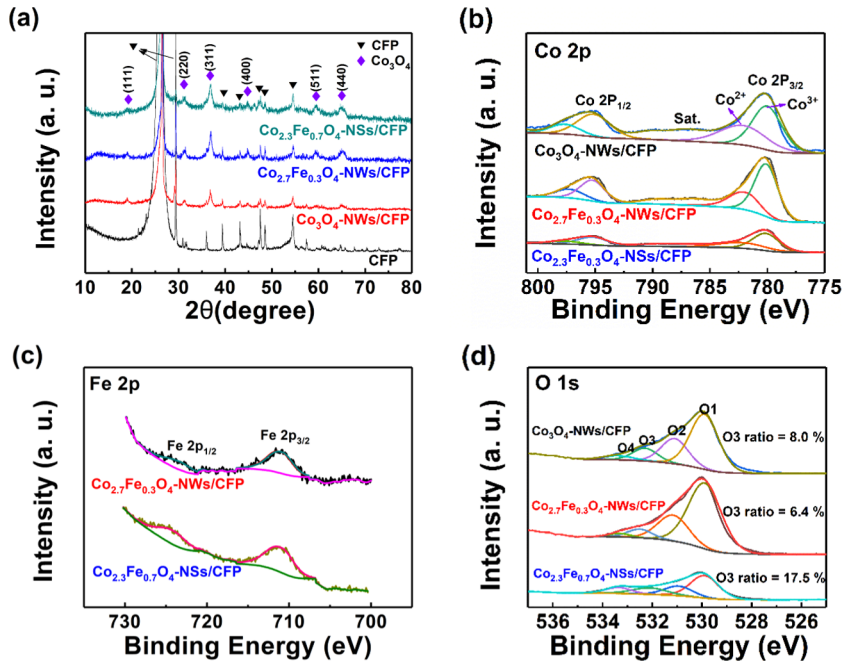

Figure 3. (a) X-ray diffraction (XRD) patterns of the CFP, Co_3O_4-NWs/CFP, $Co_{2.7}Fe_{0.3}O_4$-NWs/CFP, and $Co_{2.3}Fe_{0.7}O_4$-NSs/CFP composites. X-ray photoelectron spectroscopy (XPS) images of (b) Co 2p, (c) Fe 2p, and (d) O 1s of the Co_3O_4-NWs/CFP, $Co_{2.7}Fe_{0.3}O_4$-NWs/CFP, and $Co_{2.3}Fe_{0.7}O_4$-NSs/CFP.

support, the composite electrodes exhibit excellent electrocatalytic activity at large current densities for electrocatalytic OER.

2. RESULTS AND DISCUSSION

Scheme 1 exhibits the fabrication procedure of the $Co_xFe_{3-x}O_4$-NWs/CFP and $Co_xFe_{3-x}O_4$-NSs/CFP composite electrodes. The CFP that consists of carbon fibers with a diameter (5−10 μm) was employed as the support substrate (see Figure S1). The arrays of $Co_xFe_{3-x}O_4$ nanowires (NWs) and nanosheets were homogeneously grown and formed on the surface of carbon fibers using facile hydrothermal synthesis and thermal decomposition methods.[4,6,37,38] The morphologies and the thicknesses of $Co_xFe_{3-x}O_4$ nanoarrays can be well controlled by varying the concentration of hydrosolvent. With increasing the Fe^{3+} concentration in the hydrosolvent, the morphology of $Co_xFe_{3-x}O_4$ nanoarrays gradually changed from nanowires to nanosheets. All of the $Co_xFe_{3-x}O_4$ nanowires/nanosheets have strong interface connection with the CFP substrate, resulting in the high robustness of $Co_xFe_{3-x}O_4$ nanowires/nanosheets during the OER process at large current densities. Moreover, these kinds of one- and two-dimensional nanoarray architectures favorably facilitate the electrolyte

DOI: 10.1021/acsami.8b15357
ACS Appl. Mater. Interfaces 2018, 10, 39809−39818

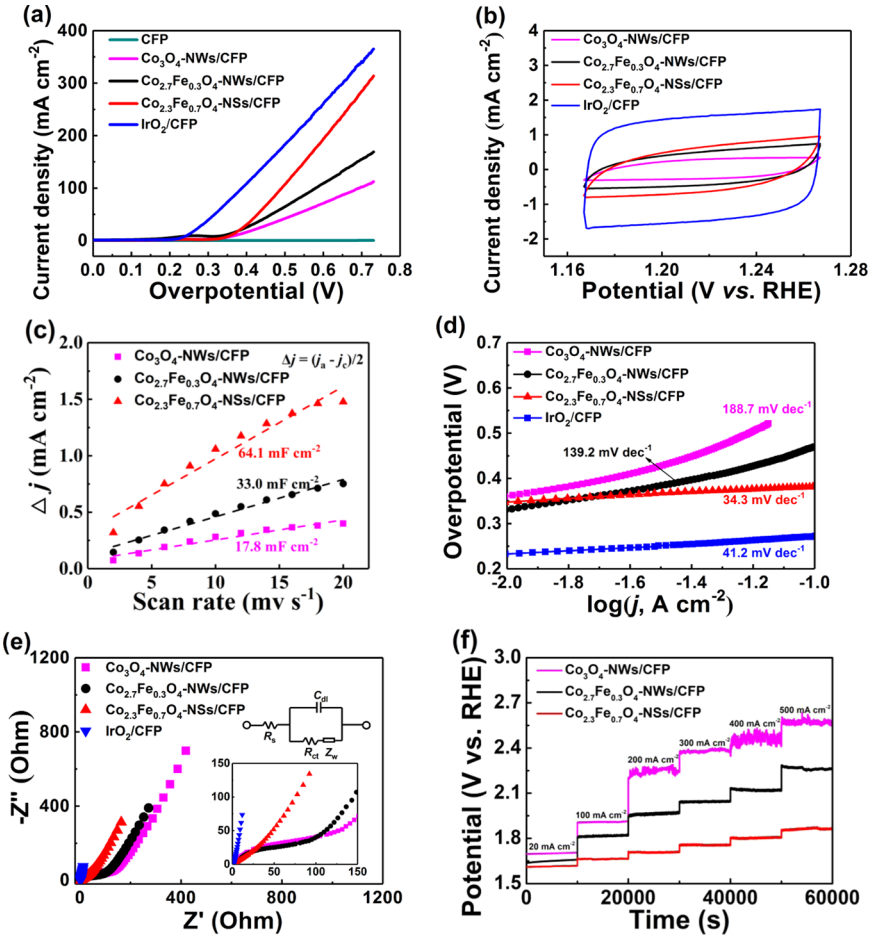

Figure 4. (a) LSV curves of the Co_3O_4-NWs/CFP, $Co_{2.7}Fe_{0.3}O_4$-NWs/CFP, $Co_{2.3}Fe_{0.7}O_4$-NSs/CFP, and IrO_2/CFP composite electrodes measured with a scan rate of 5 mV s^{-1} in 1 M KOH medium. (b) CV curves of the nanocomposite electrodes with a scan rate of 10 mV s^{-1} in 1 M KOH medium. (c) C_{dl} of the nanocomposite electrodes. (d) iR_s-corrected Tafel slopes of the nanocomposite electrodes. (e) Nyquist plots of the nanocomposite electrodes (Z'' is the imaginary impedance, and Z' is the real impedance). The inset exhibits the magnified plots in the region of high frequency. (f) Chronopotentiometric curves obtained with the nanocomposite electrodes in 1 M KOH medium at current densities of 20, 100, 200, 300, 400, and 500 mA cm^{-2}, every 10 000 s.

infiltration onto the active sites, thus increasing the electrochemically active surface area (ECSA) for the OER.

Figure 1 displays the highly homogeneous $Co_xFe_{3-x}O_4$ nanowire ($Co_xFe_{3-x}O_4$-NWs/CFP) and $Co_xFe_{3-x}O_4$ nanosheet ($Co_xFe_{3-x}O_4$-NSs/CFP) arrays grown on CFP, which are achieved through the precise control of the metal-ion concentration in the hydrosolvent. The Fe/Co molar ratios of $Co_xFe_{3-x}O_4$-NWs/CFP and $Co_xFe_{3-x}O_4$-NSs/CFP composites are approximately 1/8 and 3/10, respectively, corresponding to $Co_{2.7}Fe_{0.3}O_4$-NWs/CFP and $Co_{2.3}Fe_{0.7}O_4$-NSs/CFP composites (see Table S1 and Figure S2). It is revealed that the Fe^{3+} concentration in the hydrosolvent has a large influence on the morphology of $Co_xFe_{3-x}O_4$ nanoarrays. When the Fe^{3+} concentration was set to zero, pure Co_3O_4 nanowires were homogeneously formed on the surface of carbon fibers (see Figure S3), which is consistent with the literature.[39] When the Fe^{3+} concentration was increased to 0.1 M, the resultant $Co_{2.7}Fe_{0.3}O_4$ still maintained the morphology of the nanowire, as shown in Figure 1a–c. The $Co_{2.7}Fe_{0.3}O_4$ nanowires with a diameter of approximately 100 nm (see Figure 2a) were homogeneously grown on the surface of carbon fibers. High-resolution transmission electron microscopy (HRTEM) and selected area electron diffraction (SAED) images (see Figure 2b,c) of the multicrystalline $Co_{2.7}Fe_{0.3}O_4$ nanowires show the presence of lattice fringes and diffraction rings indexed as the (111), (220), (311), (511), and (440) crystal faces of spinel Co_3O_4, which is coincident with the analysis in Figure 3a. When the Fe^{3+} concentration was increased to 0.3 M in the hydrosolvent, the morphology of $Co_xFe_{3-x}O_4$ changed from nanowires to nanosheets. The $Co_{2.3}Fe_{0.7}O_4$ nanosheets with ultrathin thickness (see Figures 1d–f and 2d) were homogeneously formed on the surface of carbon fibers. HRTEM and SAED images (see Figure 2e,f) of the multicrystalline $Co_{2.3}Fe_{0.7}O_4$ nanosheets exhibit the lattice fringes and diffraction rings indexed as the (220), (511), and (440) crystal faces of spinel Co_3O_4, which is coincident with the analysis in Figure 3a. The morphologies of the as-prepared $Co_xFe_{3-x}O_4$ nanowire and nanosheet arrays grown on CFP in this work are more homogeneous than those of CoFe compound nanoarrays grown on other substrates (such as Ni foam and Cu foam) in the literature,[38,40] which is beneficial to the electrochemical stability of composite electrodes.

Figure 3a exhibits the XRD patterns of the CFP, Co_3O_4-NWs/CFP, $Co_{2.7}Fe_{0.3}O_4$-NWs/CFP, and $Co_{2.3}Fe_{0.7}O_4$-NSs/CFP composites. For comparison, the CFP and the Co_3O_4-NWs/CFP composite (see Figure S3) are also measured. The diffraction peaks of the CFP substrate appearing at 26.4, 29.4, 36.0, 39.5, 43.2, 47.5, and 54.5° originated from the CFP

DOI: 10.1021/acsami.8b15357
ACS Appl. Mater. Interfaces 2018, 10, 39809–39818

substrate, corresponding to two kinds of diffraction peaks of carbon including Graphite-2H (JCPDS No. 41-1487) and Chaoite [NR] (JCPDS No. 22-1069). Except for these diffraction peaks of the substrate, the diffraction peaks of the Co_3O_4-NWs/CFP, $Co_{2.7}Fe_{0.3}O_4$-NWs/CFP, and $Co_{2.3}Fe_{0.7}O_4$-NSs/CFP composites located at 19.1, 31.3, 36.8, 44.7, 59.3, and 65.2° correspond to the (111), (220), (311), (400), (511), and (440) crystal faces of spinel Co_3O_4 (JCPDS No. 42-1467). Clearly, no other diffraction peaks are discovered in the XRD patterns of the $Co_{2.7}Fe_{0.3}O_4$-NWs/CFP and $Co_{2.3}Fe_{0.7}O_4$-NSs/CFP composites except for that of the CFP and Co_3O_4. Combined with the energy-dispersive X-ray spectroscopy (EDS) analysis (Table S1 and Figure S2), it is clear that Fe species have been doped into the crystalline structure of spinel $Co_xFe_{3-x}O_4$, indicating the formation of composite nanowires and nanosheets of binary metal oxides. These consequences prove that the incorporation of Fe atoms has almost no change in the crystal structure of spinel Co_3O_4.[38] The texture coefficients of crystal facets (TC (*hkl*)) can reflect the preferred crystalline orientation of $Co_xFe_{3-x}O_4$ nanowire and nanosheet. The TC (*hkl*) values of different facets in the Co_3O_4-NWs, $Co_{2.7}Fe_{0.3}O_4$-NWs, and $Co_{2.3}Fe_{0.7}O_4$-NSs are shown in Figure S4. The TC (*hkl*) values of the (111) and (400) facets of $Co_{2.3}Fe_{0.7}O_4$-NSs have an obvious variation compared to those of Co_3O_4-NWs and $Co_{2.7}Fe_{0.3}O_4$-NWs, indicating the change of the preferred crystalline orientation to a certain extent. The preferred crystalline orientation of $Co_{2.3}Fe_{0.7}O_4$-NSs is the (400) plane, rather than the (111) plane for Co_3O_4-NWs and $Co_{2.7}Fe_{0.3}O_4$-NWs. Moreover, the morphology change may be the consequence of the variation of the preferred growth orientation with increasing Fe^{3+} concentration, which is similar to the change of the preferred crystalline orientation (see Figure S4).

Figure 3b–d displays the XPS images of the Co_3O_4-NWs/CFP, $Co_{2.7}Fe_{0.3}O_4$-NWs/CFP, and $Co_{2.3}Fe_{0.7}O_4$-NSs/CFP. Clearly, the overall XPS images of $Co_{2.7}Fe_{0.3}O_4$-NWs/CFP and $Co_{2.3}Fe_{0.7}O_4$-NSs/CFP definitely exhibit the existence of Co, Fe, and O elements, further confirming the introduction of Fe ion. The Co 2p spectra of the samples in Figure 3b present doublets at 780.3 and 795.57 eV that correspond to Co $2p_{3/2}$ and Co $2p_{1/2}$. The Co $2p_{3/2}$ spectra can be divided into two fitting peaks of Co^{2+} (782.2 eV) and Co^{3+} (780.1 eV), which is consistent with the valence states of Co species in spinel Co_3O_4. The Fe 2p spectra of the $Co_{2.7}Fe_{0.3}O_4$-NWs/CFP and $Co_{2.3}Fe_{0.7}O_4$-NSs/CFP in Figure 3c exhibit pairs of peaks located at 725.2 and 711.5 eV, with a spin-energy separation of 13.7 eV, corresponding to the Fe $2p_{1/2}$ and Fe $2p_{3/2}$ signals. The O 1s spectra of the Co_3O_4-NWs/CFP, $Co_{2.7}Fe_{0.3}O_4$-NWs/CFP, and $Co_{2.3}Fe_{0.7}O_4$-NSs/CFP in Figure 3d can be decomposed into four characteristic peaks that resulted from metal-oxygen bounds (529.9 eV for O1), defective oxygen sites with a low coordination number (531.1 eV for O2), hydroxyl groups or surface-absorbed oxygen (532.3 eV for O3), and adsorbed molecular water (533.4 eV for O4).[25,41] Interestingly, the $Co_{2.3}Fe_{0.7}O_4$-NSs/CFP has a higher O3 ratio (17.5%) compared to Co_3O_4-NWs/CFP (8.0%) and $Co_{2.7}Fe_{0.3}O_4$-NWs/CFP (6.4%). This consequence indicates that the different morphologies and Fe contents in $Co_xFe_{3-x}O_4$ nanoarrays can result in different surface characteristics that are very important to the adsorption of intermediate products (OH*, O_2*, O*, and OOH*) for the OER, especially the hydroxyl groups (O3).[42−44] All of the highly recognized mechanisms for the OER in alkaline conditions involve in the elementary step that is the adsorption−desorption of $O\bar{H}$ ion on the surface of active site (S).[45] The elementary step is given below

$$S + OH^-(aq) \rightarrow S - OH + e^- \quad (1)$$

Undoubtedly, the surface of the $Co_{2.3}Fe_{0.7}O_4$-NSs/CFP with a high O3 ratio (17.5%) possesses more active sites to adsorb hydroxide ion and finish the OER, indicating higher ECSA and electrocatalytic activity in comparison with Co_3O_4-NWs/CFP and $Co_{2.7}Fe_{0.3}O_4$-NWs/CFP.

Figure 4a exhibits the linear sweep voltammetry (LSV) curves of the Co_3O_4-NWs/CFP, $Co_{2.7}Fe_{0.3}O_4$-NWs/CFP, $Co_{2.3}Fe_{0.7}O_4$-NSs/CFP, and IrO_2/CFP composite electrodes at a scan rate of 5 mV s^{-1} in a 1 M KOH medium. As shown in the figure, the current density of the bare CFP for the OER is considerably lower than that of the $Co_xFe_{3-x}O_4$-loaded composite electrodes. The onset overpotentials of the Co_3O_4-NWs/CFP, $Co_{2.7}Fe_{0.3}O_4$-NWs/CFP, $Co_{2.3}Fe_{0.7}O_4$-NSs/CFP, and IrO_2/CFP composite electrodes were 181, 166, 169, and 91 mV, respectively. The overpotentials of the OER at 10 mA cm^{-2} for the Co_3O_4-NWs/CFP, $Co_{2.7}Fe_{0.3}O_4$-NWs/CFP, $Co_{2.3}Fe_{0.7}O_4$-NSs/CFP, and IrO_2/CFP composite electrodes were 372, 342, 359, and 245 mV, respectively. Clearly, the onset overpotentials and overpotentials at 10 mA cm^{-2} of the Fe-doped Co_3O_4 nanoarray electrodes are lower than those of the clean Co_3O_4 nanoarray electrode. The $Co_{2.3}Fe_{0.7}O_4$-NSs/CFP composite electrode at an OER overpotential of 500 mV can reach a higher current density (106.8 mA cm^{-2}) than that of $Co_{2.7}Fe_{0.3}O_4$-NWs/CFP (64.4 mA cm^{-2}) and Co_3O_4-NWs/CFP (42.0 mA cm^{-2}). It is obvious that the current densities of $Co_{2.7}Fe_{0.3}O_4$-NWs/CFP and $Co_{2.3}Fe_{0.7}O_4$-NSs/CFP composite electrodes at the same OER overpotential are higher than those for Co_3O_4-NWs/CFP composite electrode, indicating that the Fe doping in the pristine Co_3O_4 nanostructures can greatly improve the electrocatalytic activity. Figure 4b exhibits the cyclic voltammetry (CV) curves of the samples performed in the potential region (1.167−1.267 V vs reversible hydrogen electrode (RHE)) with a scan rate of 10 mV s^{-1} in a 1 M KOH solution. Clearly, the regulation for the current density values of anode (j_a) and cathode (j_c) of these samples is homologous to that of the OER current densities under the same overpotential in Figure 4a. The electrocatalytic activity of nanocomposite electrodes was further evaluated by the ECSA. The double-layer capacitance (C_{dl}) is proportional to ECSA, which is generally used to evaluate the effective ECSA. The C_{dl} evaluation for the ECSA of these samples is only qualitative owing to the pseudocapacitance characteristic for these metal-based oxides.[18,46−48] The CV curves were recorded in the nonfaradic range (1.167−1.267 V vs RHE) within the scan rate region (2−20 mV s^{-1}). Figure 4c exhibits the capacitance currents of these nanocomposite electrodes with scan rate. The C_{dl} of the nanocomposite electrodes was obtained by fitting a linear regression according to the capacitance currents of the CV curves in Figure S5. The C_{dl} of the Co_3O_4-NWs/CFP, $Co_{2.7}Fe_{0.3}O_4$-NWs/CFP, and $Co_{2.3}Fe_{0.7}O_4$-NSs/CFP composite electrodes are 17.8, 33.0, and 64.1 mF cm^{-2}, respectively, indicating that the $Co_{2.3}Fe_{0.7}O_4$-NSs/CFP composite electrode has the highest effective ECSA among these samples. Figure S6 shows the N_2 adsorption/desorption isotherms of the Co_3O_4-NWs/CFP, $Co_{2.7}Fe_{0.3}O_4$-NWs/CFP, and $Co_{2.3}Fe_{0.7}O_4$-NSs/CFP composites. The curve of these samples shows an obvious hysteresis loop from P/P_0 = 0.4 to 0.99, which belong to a

DOI: 10.1021/acsami.8b15357
ACS Appl. Mater. Interfaces 2018, 10, 39809−39818

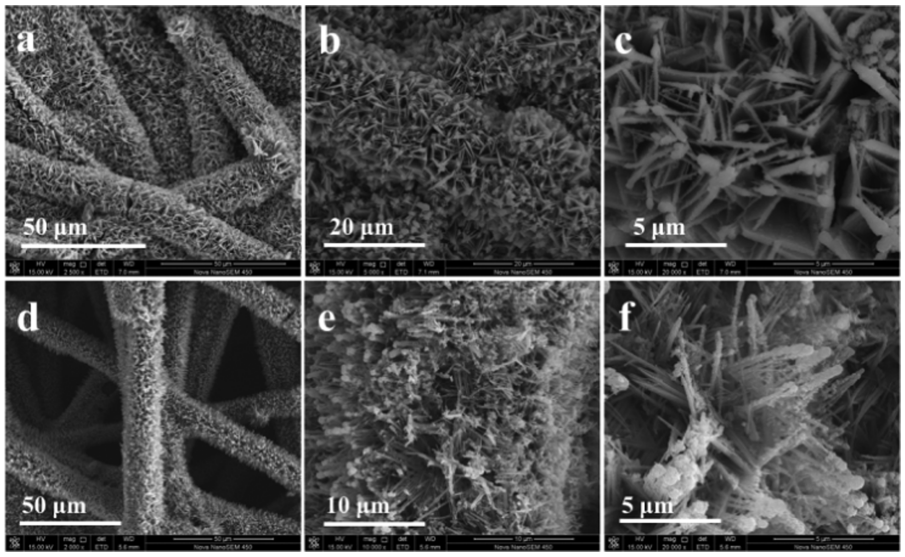

Figure 5. FESEM images showing the morphologies of (a–c) $Co_{2.3}Fe_{0.7}O_4$-NSs/CFP and (d–f) $Co_{2.7}Fe_{0.3}O_4$-NWs/CFP composites after electrochemical OER for 100 h at 1000 mA cm^{-2}.

typical IV-type isotherm.[49−51] This indicates that mesopores (2–50 nm) are dominant in these nanocomposites. Table S2 exhibits that the Brunauer–Emmett–Teller (BET) specific surface area of $Co_{2.3}Fe_{0.7}O_4$-NSs/CFP (18.2 m^2 g^{-1}) is higher than that of Co_3O_4-NWs/CFP (7.6 m^2 g^{-1}) and $Co_{2.7}Fe_{0.3}O_4$-NWs/CFP (4.5 m^2 g^{-1}), which should be the consequence of the lower average pore size. These BET data are consistent with the C_{dl} values of the nanocomposite electrodes in Figure 4c. These data clearly indicate that the $Co_{2.3}Fe_{0.7}O_4$-NS arrays have much superior electrocatalytic activity compared to the Co_3O_4-NW and $Co_{2.7}Fe_{0.3}O_4$-NW nanoarrays. This consequence should be attributed to the morphology of the $Co_{2.3}Fe_{0.7}O_4$-NSs/CFP that can provide more surface active sites and higher Fe-doping content.

For photoelectrochemical water splitting, the onset potential and the OER overpotential at 10 mA cm^{-2} are the key parameters to evaluate the properties of electrocatalysts because the current densities are relatively low in the application scenario.[41,52] However, for electrochemical water splitting, the current densities are normally much higher (>500 mA cm^{-2}) to fulfill industrial demands.[2] Hence, to reasonably assess the electrode performance for electrocatalytic OER, the onset potential and the overpotential are not enough. Tafel slopes are usually employed to identify the reaction kinetics of electrodes and can therefore serve as a crucial parameter for electrocatalytic OER, especially at large current densities. Typically, the smaller the Tafel slopes, the higher the OER current densities at the same overpotential. Figure 4d shows the iR_s-corrected Tafel plots of the samples derived from the LSVs in Figure 4a. For accurate comparison of Tafel plots, the R_s of all of the electrodes was taken as the same value of 1.1 Ω, and the Tafel slopes were calculated in an appropriate range of current densities. As shown in Figure 4d, the $Co_{2.3}Fe_{0.7}O_4$-NSs/CFP composite electrode has a lower Tafel slope (34.3 mV dec^{-1}) than Co_3O_4-NWs/CFP (188.7 mV dec^{-1}), $Co_{2.7}Fe_{0.3}O_4$-NWs/CFP (139.2 mV dec^{-1}), and IrO_2/CFP (41.2 mV dec^{-1}). This should be attributed to the higher ECSA and a high O3 ratio of $Co_{2.3}Fe_{0.7}O_4$-NSs/CFP for the adsorption of intermediate products. Table S3 exhibits the electrocatalytic activities for some advanced electrodes for OER. The OER overpotential of the $Co_{2.3}Fe_{0.7}O_4$-NSs/CFP electrode at a current density of 10 mA cm^{-2} is comparable to these electrodes, as shown in the table. It is also obvious that the $Co_{2.3}Fe_{0.7}O_4$-NSs/CFP electrode possesses a much lower Tafel slope of 34.3 mV dec^{-1} than these advanced materials, indicating the superior electrocatalytic activity at large current density of electrochemical water splitting.

Figure 4e shows the Nyquist plots of these composite electrodes. The equivalent circuit, $R_s(C_{dl}(R_{ct}Z_w))$, is used to fit the electrochemical impedance spectroscopy (EIS) data of these nanocomposite electrodes for OER, which has been inserted in the figure.[53,54] R_s corresponds to the bulk solution resistance, C_{dl} represents the double-layer capacitance, R_{ct} corresponds to the charge-transfer resistance, and Z_w is the Warburg resistance. The fitted EIS data for these electrodes are exhibited in Table S4. As shown in the table, R_{ct} of $Co_{2.3}Fe_{0.7}O_4$-NSs/CFP (10.3 Ω cm^{-2}) for the OER is lower than that of Co_3O_4-NWs/CFP (50.3 Ω cm^{-2}) and $Co_{2.7}Fe_{0.3}O_4$-NWs/CFP (40.9 Ω cm^{-2}), indicating that more excellent electrocatalytic activity resulted from the higher Fe-doping content.[18]

Figure 4f shows continuous multistep chronopotentiometric curves in a 1 M KOH solution. These nanocomposite electrodes are subjected to a long-term OER of 60 000 s at different current densities (20–500 mA cm^{-2}). As shown in the figure, the OER potential of the $Co_{2.3}Fe_{0.7}O_4$-NSs/CFP composite electrode is much lower than that of Co_3O_4-NWs/CFP and $Co_{2.7}Fe_{0.3}O_4$-NWs/CFP at the same current density. It is also obvious that the OER potential of the $Co_{2.3}Fe_{0.7}O_4$-NSs/CFP composite electrode has a very small fluctuation during the 60 000 s electrolysis at different current densities, indicating the excellent OER stability. In contrast, the Co_3O_4-NWs/CFP electrode has very large fluctuation of the potential at current densities ≥200 mA cm^{-2} with time. The current–time chronoamperometric responses further confirm the excellent OER stability of the $Co_{2.3}Fe_{0.7}O_4$-NSs/CFP electrode with higher OER current density compared to the Co_3O_4-NWs/CFP and $Co_{2.7}Fe_{0.3}O_4$-NWs/CFP electrodes (see Figure S7). These chronopotentiometric responses reflect higher OER stability and better mass transport characteristics

DOI: 10.1021/acsami.8b15357
ACS Appl. Mater. Interfaces 2018, 10, 39809–39818

(external diffusion of O_2 bubbles and inner diffusion of OH^-), mechanical robustness, and conductivity of the $Co_{2.3}Fe_{0.7}O_4$-NSs/CFP nanocomposite electrode compared to Co_3O_4-NWs/CFP and $Co_{2.7}Fe_{0.3}O_4$-NWs/CFP.

The OER stability of the electrodes at large current densities for electrochemical water splitting is very important due to the requirements for industrial applications. It is obvious that the $Co_{2.3}Fe_{0.7}O_4$-NSs/CFP composite electrode for the OER possesses outstanding long-term stability at large current densities (see Table S3). Figure 5 shows the morphologies of the $Co_{2.7}Fe_{0.3}O_4$-NWs/CFP and $Co_{2.3}Fe_{0.7}O_4$-NSs/CFP composite electrodes after electrochemical OER for 100 h at a current density of 1000 mA cm^{-2}. The nanosheet array morphology of the $Co_{2.3}Fe_{0.7}O_4$-NSs/CFP composite electrode in Figure 5a–c showed almost no change compared to the fresh electrode in Figure 2d–f, indicating its high stability at a high current density. However, the morphology of the $Co_{2.7}Fe_{0.3}O_4$-NWs/CFP was changed to a certain extent (Figure 5d–f). It was also discovered that the Fe contents in $Co_{2.7}Fe_{0.3}O_4$-NWs/CFP and $Co_{2.3}Fe_{0.7}O_4$-NSs/CFP relatively decreased after the OER for 100 h (see Table S1, Figure S2, Table S5, and Figure S8). Figure S9 exhibits the XRD patterns of the samples after the OER for 100 h at 1000 mA cm^{-2}. The $Co_xFe_{3-x}O_4$ nanowire/nanosheet after the OER for 100 h still well maintained the crystalline structure of spinel Co_3O_4. However, the diffraction peak of the Co_3O_4 (440) crystal face for the $Co_{2.7}Fe_{0.3}O_4$-NWs/CFP composite electrode appearing at 65.2° greatly decreased compared to the fresh electrode, but that for the $Co_{2.3}Fe_{0.7}O_4$-NSs/CFP composite electrode had nearly no variation. This result indicates that the $Co_{2.3}Fe_{0.7}O_4$ nanosheet has higher structure and composition stability than the $Co_{2.7}Fe_{0.3}O_4$ nanowire during the long-term OER at large current densities. Figure S10 shows the XPS images of $Co_{2.7}Fe_{0.3}O_4$-NWs/CFP and $Co_{2.3}Fe_{0.7}O_4$-NSs/CFP corresponding to the fresh electrodes and the electrodes after electrochemical OER for 100 h at 1000 mA cm^{-2}. It is discovered that the Fe 2p spectra of fresh $Co_{2.3}Fe_{0.7}O_4$-NSs/CFP and after 100 h of the OER in Figure S10c had almost no change, indicating a small variation of the Fe-doping content on the $Co_{2.3}Fe_{0.7}O_4$-NS surface. However, the Fe spectra of the $Co_{2.7}Fe_{0.3}O_4$-NWs/CFP after 100 h of electrocatalytic OER nearly vanished compared to those of the fresh electrode, indicating the removal of Fe atoms on the $Co_{2.7}Fe_{0.3}O_4$-NW surface. This reason should be the consequence of the variation of the preferred crystalline orientation (Figure S4), indicating that $Co_{2.3}Fe_{0.7}O_4$-NSs can more effectively preserve the Fe species on the exposed facets compared to $Co_{2.3}Fe_{0.7}O_4$-NW. It is also discovered that $Co_{2.7}Fe_{0.3}O_4$-NWs/CFP and $Co_{2.3}Fe_{0.7}O_4$-NSs/CFP have a large change in the content ratios of O1, O2, O3, and O4, indicating the variation of surface characteristics for the adsorption of intermediate products after long-term OER (Figure S10e).[40−42]

Generally, the electrochemical stability of active materials and the surface passivation of support materials are the main factors of the OER stability for metal-based oxide electrodes.[54,55] However, the OER stability of nanostructural materials is different from that of the traditional precious metal oxide electrocatalysts. In this study, the high stability of the $Co_{2.3}Fe_{0.7}O_4$-NSs/CFP composite electrodes at large OER current densities should be attributed to several key factors: (1) the CFP substrate possesses high corrosion resistance and excellent electrical properties, which make it suitable to serve as the support substrate of nanoarrays for the OER. Unlike the metal substrate, the CFP hardly passivates under high overpotential during long-term OER. (2) The highly homogeneous $Co_{2.3}Fe_{0.7}O_4$-NS arrays grown on CFP have high robustness and strong interface connection with the CFP substrate, which make them ultrastable even under strong OER (>500 mA cm^{-2}). (3) Compared to $Co_{2.7}Fe_{0.3}O_4$-NWs, $Co_{2.3}Fe_{0.7}O_4$-NSs have higher structure and composition stability during the long-term OER at large current densities, owing to the change of the preferred crystalline orientation. Consequently, the $Co_xFe_{3-x}O_4$-NSs/CFP composite electrodes have excellent electrocatalytic activity and superior stability compared to RuO_2- and IrO_2-based electrocatalysts.[34−36,56,57]

3. CONCLUSIONS

To summarize, ultrathin $Co_xFe_{3-x}O_4$ nanosheet/nanowire arrays grown on CFP for the electrocatalytic OER were successfully fabricated. The incorporation of Fe atoms into the spinel Co_3O_4 and the ultrathin nanosheet morphology can greatly improve the electrocatalytic activity and OER stability at large current densities. The $Co_{2.3}Fe_{0.7}O_4$-NSs/CFP composite electrode for the OER exhibited a small value of Tafel slope (34.3 mV dec^{-1}) and superior stability at the current density of 1000 mA cm^{-2} for 100 h without a morphology change. The fabrication of the $Co_{2.3}Fe_{0.7}O_4$-NSs/CFP electrode for the electrochemical OER provides new insights to design nonprecious, highly active, and stable metal oxide composite electrodes for the possibility of large-scale practical applications.

4. EXPERIMENTAL SECTION

4.1. Chemicals. All of the chemicals of analytical grade were supplied by Aladdin Chemistry Co. (Shanghai, China) and used as raw materials for the electrode preparation without further purification.

4.2. Electrode Preparation. A CFP (TGH-060, Toray Industries Co., Ltd.) was cut into pieces of 10 mm × 60 mm × 0.33 mm and employed as the support substrate for the fabrication of the nanoarray composite electrodes. The pieces of CFP were subjected to surface pretreatments by ethanol, 0.1 M H_2SO_4 medium, and deionized water in sequence for 10 min in an ultrasonic water bath. Meanwhile, the mixed hydrosolvents of $Co(NO_3)_2{\cdot}6H_2O$, $Fe(NO_3)_3{\cdot}9H_2O$, $CO(NH_2)_2$, and NH_4F with different concentrations were prepared in 80 mL of deionized water (see Table S6). The concentration parameters for the fabrication of Co_3O_4 nanowire (Co_3O_4-NWs/CFP), $Co_xFe_{3-x}O_4$ nanowire ($Co_{2.7}Fe_{0.3}O_4$-NWs/CFP), and $Co_xFe_{3-x}O_4$ ($Co_{2.3}Fe_{0.7}O_4$-NSs/CFP) nanosheet arrays grown on CFP correspond to the Fe/Co molar ratios of 0, 1/3.74, and 3/3.74 in the hydrosolvents (see Table S6). The hydrosolvent was poured into a Teflon-lined stainless steel autoclave, and the CFP was completely immersed in the solution. The autoclave was sealed and heated in a furnace at 120 °C for 3–7 h and then naturally cooled to room temperature. After the hydrothermal process, the CFP was taken out and washed with water several times. After drying at 60 °C, the $Co_xFe_{1-x}(OH)(CO_3)_{0.5}$ nanoarrays were successfully synthesized on CFP.[6,34−36] The dried $Co_xFe_{1-x}(OH)(CO_3)_{0.5}$ nanoarray composite electrodes were then heated in air at 350 °C for 2 h to fully convert into crystalline $Co_xFe_{3-x}O_4$ nanoarrays. All of the nanocomposite electrodes ensure an approximate loading of active material (4–5 mg cm^{-2}). For comparison, the IrO_2/CFP composite electrode was also fabricated using the method of thermal decomposition according to the previous method.[18]

4.3. Material Characterizations. The crystallinity of these nanocomposite electrodes was identified by X-ray diffraction (XRD, D8 Advance-A25). Field emission scanning electron microscopy (FESEM, Zeiss Supra-55), transmission electron microscopy (TEM, FEIG2-20-TWIN), and energy-dispersive X-ray spectroscopy (EDS,

DOI: 10.1021/acsami.8b15357
ACS Appl. Mater. Interfaces 2018, 10, 39809−39818

Oxford Instruments) were employed to analyze the morphologies and compositions of the nanocomposite electrodes. The valence states of the $Co_xFe_{3-x}O_4$ nanoarrays were measured using X-ray photoelectron spectroscopy (XPS) with an Axis Ultra DLD electron spectrometer (Shimadzu-Kratos) at 150 W Al Kα radiation. An analytical balance (Mettler Toledo, XS205 Dual Range) was employed to weigh the loading amounts of active materials on CFP.

4.4. Electrochemical Characterizations. An electrochemical workstation (CHI 660D, CH Instruments Inc.) with a three-electrode configuration was used to perform the electrochemical behavior of these samples in a 1 M KOH medium at 25 °C. A saturated calomel electrode was calibrated to the reversible hydrogen electrode (RHE), which was employed as the reference electrode.[18] The nanocomposite electrodes with a geometric area (10 mm × 10 mm) were used as the working electrodes, and the auxiliary electrode was a Pt foil. Linear sweep voltammetry (LSV) curves of the samples were performed at a scan rate of 5 mV s^{-1}. Electrochemical impedance spectroscopy (EIS) was carried out in the frequency region of 100 kHz to 10 mHz at a potential (1.070 V vs RHE) of the C_{dl} region using a 5 mV signal. The corresponding Tafel plots for the collected iR_s drop were obtained. The iR_s drop is derived from the EIS, where i corresponds to the faradic current of LSV and R_s represents the electrolyte resistance that is determined by the X axis intercepts of the Nyquist plots. The chronopotentiometric curves for these nanocomposite electrodes were obtained under the same experimental setup of a three-electrode configuration with compensating iR_s drop in a 1 M KOH medium. The long-term OER stabilities for the nanocomposite electrodes were measured with 1000 mA cm^{-2} in the 1 M KOH medium at room temperature. The different nanoarray electrodes were applied as the anode, and pure titanium plate with a size of 40 mm × 40 mm was used as the cathode, which assembled a cell for electrochemical water splitting.

■ ASSOCIATED CONTENT

Supporting Information

The Supporting Information is available free of charge on the ACS Publications website at DOI: 10.1021/acsami.8b15357.

FESEM images, EDS mappings, TC (*hkl*) values, CV curves, N_2 adsorption−desorption isotherms, XRD patterns, XPS images (Figures S1−S10); normalized atomic ratios, summary of specific surface area, pore size and pore volume, comparison of electrocatalytic activities, normalized atomic ratios of Co and Fe, and influence of reagent concentrations (Tables S1−S6) (PDF)

■ AUTHOR INFORMATION

Corresponding Authors

*E-mail: yezhiguo2008@163.com (Z.Y.).
*E-mail: zhongjin@nju.edu.cn (Z.J.).

ORCID

Zhiguo Ye: 0000-0002-2669-8182
Duosheng Li: 0000-0003-1299-5554
Zhong Jin: 0000-0001-8860-8579

Notes

The authors declare no competing financial interest.

■ ACKNOWLEDGMENTS

This work was supported by the National Natural Science Foundation of China (51862026, 51562027, 21573108, and 51761135104), the National Key R&D Program of China (2017YFA0208200 and 2016YFB0700600), the Aeronautical Science Foundation of China (2017ZF56027), the Programme for Innovation of Science and Technology of Shanxi Province (2015KTZDSF-02-02), and the excellent Youth Foundation of Jiangxi Scientific Committee (20171BCB23054).

■ REFERENCES

(1) Smith, R. D. L.; Prévot, M. S.; Fagan, R. D.; Zhang, Z.; Sedach, P. A.; Siu, M. K. J.; Trudel, S.; Berlinguette, C. P. Photochemical Route for Accessing Amorphous Metal Oxide Materials for Water Oxidation Catalysis. *Science* **2013**, *340*, 60−63.

(2) Lu, X.; Zhao, C. Electrodeposition of Hierarchically Structured Three-Dimensional Nickel-Iron Electrodes for Efficient Oxygen Evolution at High Current Densities. *Nat. Commun.* **2015**, *6*, No. 6616.

(3) Luan, C. L.; Liu, G. L.; Liu, Y. J.; Yu, L.; Wang, Y.; Xiao, Y.; Qiao, H. Y.; Dai, X. P.; Zhang, X. Structure Effects of 2D Materials on α-Nickel Hydroxide for Oxygen Evolution Reaction. *ACS Nano* **2018**, *12*, 3875−3885.

(4) Wang, K.; Ye, Z. G.; Liu, C. Q.; Xi, D.; Zhou, C. J.; Shi, Z. Q.; Xia, H. Y.; Liu, G. W.; Qiao, G. J. Morphology-Controllable Synthesis of Cobalt Telluride Branched Nanostructures on Carbon Fiber Paper as Electrocatalysts for Hydrogen Evolution Reaction. *ACS Appl. Mater. Interfaces* **2016**, *8*, 2910−2916.

(5) Huang, Y. Y.; Yang, R.; Anandhababu, G.; Xie, J. F.; Lv, J. Q.; Zhao, X. T.; Wang, X. Y.; Wu, M. X.; Li, Q. H.; Wang, Y. B. Cobalt/Iron (Oxides) Heterostructures for Efficient Oxygen Evolution and Benzyl Alcohol Oxidation Reactions. *ACS Energy Lett.* **2018**, *3*, 1854−1860.

(6) Wang, K.; Xi, D.; Zhou, C. J.; Shi, Z. Q.; Xia, H. Y.; Liu, G. W.; Qiao, G. J. $CoSe_2$ Necklace-Like Nanowires Supported By Carbon Fiber Paper: A 3D Integrated Electrode for the Hydrogen Evolution Reaction. *J. Mater. Chem. A* **2015**, *3*, 9415−9420.

(7) Liu, H. X.; Wang, Y. R.; Lu, X. Y.; Hu, Y.; Zhu, G. Y.; Chen, R. P.; Ma, L. B.; Zhu, H. F.; Tie, Z. X.; Liu, J.; Jin, Z. The Effects of Al Substitution and Partial Dissolution on Ultrathin NiFeAl Trinary Layered Double Hydroxide Nanosheets for Oxygen Evolution Reaction in Alkaline Solution. *Nano Energy* **2017**, *35*, 350−357.

(8) Yang, Y.; Fei, H. L.; Ruan, G. D.; Xiang, C. S.; Tour, J. M. Efficient Electrocatalytic Oxygen Evolution on Amorphous Nickel-Cobalt Binary Oxide Nanoporous Layers. *ACS Nano* **2014**, *8*, 9518−9523.

(9) Anandhababu, G.; Huang, Y. Y.; Babu, D. D.; Wu, M. X.; Wang, Y. B. Oriented Growth of ZIF-67 to Derive 2D Porous CoPO Nanosheets for Electrochemical-/Photovoltage-Driven Overall Water Splitting. *Adv. Funct. Mater.* **2018**, *28*, No. 1706120.

(10) Ma, L. B.; Hu, Y.; Chen, R. P.; Zhu, G. Y.; Chen, T.; Lv, H. L.; Wang, Y. R.; Liang, J.; Liu, H. X.; Yan, C. Z.; Zhu, H. F.; Tie, Z. X.; Jin, Z.; Liu, J. Self-Assembled Ultrathin $NiCo_2S_4$ Nanoflakes Grown on Ni Foam as High-Performance Flexible Electrodes for Hydrogen Evolution Reaction in Alkaline Solution. *Nano Energy* **2016**, *24*, 139−147.

(11) Ye, Z.-G.; Meng, H.-M.; Chen, D.; Yu, H.-Y.; Fan, Z.-S.; Wang, X.-D.; Sun, D.-B. Structure and Characteristics of $Ti/IrO_2(x) + MnO_2(1-x)$ Anode for Oxygen Evolution. *Solid State Sci.* **2008**, *10*, 346−354.

(12) Dou, Y. H.; Liao, T.; Ma, Z. Q.; Tian, D. L.; Liu, Q. N.; Xiao, F.; Sun, Z. Q.; Kim, J. H.; Dou, S. X. Graphene-Like Holey Co_3O_4 Nanosheets as A Highly Efficient Catalyst for Oxygen Evolution Reaction. *Nano Energy* **2016**, *30*, 267−275.

(13) Osgood, H.; Devaguptapu, S. V.; Xu, H.; Cho, J.; Wu, G. Transition Metal (Fe, Co, Ni, and Mn) Oxides for Oxygen Reduction and Evolution Bifunctional Catalysts in Alkaline Media. *Nano Today* **2016**, *11*, 601−625.

(14) Han, L.; Dong, S.; Wang, E. Transition-Metal (Co, Ni, and Fe)-Based Electrocatalysts for the Water Oxidation Reaction. *Adv. Mater.* **2016**, *28*, 9266−9291.

(15) Liu, X.; Liu, W.; Ko, M.; Park, M.; Kim, M. G.; Oh, P.; Chae, S.; Park, S.; Casimir, A.; Wu, G.; Cho, J. Metal (Ni, Co)-Metal Oxides/Graphene Nanocomposites as Multifunctional Electrocatalysts. *Adv. Funct. Mater.* **2015**, *25*, 5799−5808.

DOI: 10.1021/acsami.8b15357
ACS Appl. Mater. Interfaces 2018, 10, 39809−39818

(16) Kargar, A.; Kim, S. J.; Allameh, P.; Choi, C.; Park, N.; Jeong, H.; Pak, Y.; Jung, G. Y.; Pan, X. Q.; Wang, D. L.; Jin, S. p-Si/SnO_2/Fe_2O_3 Core/Shell/Shell Nanowire Photocathodes for Neutral pH Water Splitting. *Adv. Funct. Mater.* **2015**, *25*, 2609−2615.
(17) Meng, Y.; Song, W.; Huang, H.; Ren, Z.; Chen, S.-Y.; Suib, S. L. Structure-Property Relationship of Bifunctional MnO_2 Nanostructures: Highly Efficient, Ultra-Stable Electrochemical Water Oxidation and Oxygen Reduction Reaction Catalysts Identified in Alkaline Media. *J. Am. Chem. Soc.* **2014**, *136*, 11452−11464.
(18) Ye, Z. G.; Li, T.; Ma, G.; Dong, Y. H.; Zhou, X. L. Metal-Ion (Fe, V, Co, and Ni)-Doped MnO_2 Ultrathin Nanosheets Supported on Carbon Fiber Paper for the Oxygen Evolution Reaction. *Adv. Funct. Mater.* **2017**, *27*, No. 1704083.
(19) Rosen, J.; Hutchings, G. S.; Jiao, F. Ordered Mesoporous Cobalt Oxide as Highly Efficient Oxygen Evolution Catalyst. *J. Am. Chem. Soc.* **2013**, *135*, 4516−4521.
(20) Jiao, F.; Frei, H. Nanostructured Cobalt Oxide Clusters in Mesoporous Silica as Efficient Oxygen-Evolving Catalysts. *Angew. Chem., Int. Ed.* **2009**, *48*, 1841−1844.
(21) Xu, Y. J.; Bian, W. Y.; Wu, J.; Tian, J. H.; Yang, R. Z. Preparation and electrocatalytic activity of 3D hierarchical porous spinel $CoFe_2O_4$ hollow nanospheres as efficient catalyst for Oxygen Reduction Reaction and Oxygen Evolution Reaction. *Electrochim. Acta* **2015**, *151*, 276−283.
(22) Yan, W. N.; Bian, W. Y.; Jin, C.; Tian, J. H.; Yang, R. Z. An Efficient Bi-functional Electrocatalyst Based on Strongly Coupled $CoFe_2O_4$/Carbon Nanotubes Hybrid for Oxygen Reduction and Oxygen Evolution. *Electrochim. Acta* **2015**, *177*, 65−72.
(23) Yuan, C. Z.; Yang, L.; Hou, L. R.; Shen, L. F.; Zhang, X. G.; Lou, X. W. Growth of Ultrathin Mesoporous Co_3O_4 Nanosheet Arrays on Ni Foam for High-Performance Electrochemical Capacitors. *Energy Environ. Sci.* **2012**, *5*, 7883−7887.
(24) Trotochaud, L.; Young, S. L.; Ranney, J. K.; Boettcher, S. W. Nickel-Iron Oxyhydroxide Oxygen-Evolution Electrocatalysts: The Role of Intentional and Incidental Iron Incorporation. *J. Am. Chem. Soc.* **2014**, *136*, 6744−6753.
(25) Zhuang, L.; Ge, L.; Yang, Y.; Li, M.; Jia, Y.; Yao, X.; Zhu, Z. Ultrathin Iron-Cobalt Oxide Nanosheets with Abundant Oxygen Vacancies for the Oxygen Evolution Reaction. *Adv. Mater.* **2017**, *29*, No. 1606793.
(26) Friebel, D.; Louie, M. W.; Bajdich, M.; Sanwal, K. E.; Cai, Y.; Wise, A. M.; Cheng, M. J.; Sokaras, D.; Weng, T. C.; Alonso-Mori, R.; Davis, R. C.; Bargar, J. R.; Nørskov, J. K.; Nilsson, A.; Bell, A. T. Identification of Highly Active Fe Sites in (Ni,Fe)OOH for Electrocatalytic Water Splitting. *J. Am. Chem. Soc.* **2015**, *137*, 1305−1313.
(27) Trześniewski, B. J.; Diaz-Morales, O.; Vermass, D. A.; Longo, A.; Bras, W.; Koper, M. T. M.; Smith, W. A. In Situ Observation of Active Oxygen Species in Fe-Containing Ni-Based Oxygen Evolution Catalysts: The Effect of pH on Electrochemical Activity. *J. Am. Chem. Soc.* **2015**, *137*, 15112−15121.
(28) Xu, K.; Chen, P.; Li, X.; Tong, Y.; Ding, H.; Wu, X.; Chu, W.; Peng, Z.; Wu, C.; Xie, Y. Metallic Nickel Nitride Nanosheets Realizing Enhanced Electrochemical Water Oxidation. *J. Am. Chem. Soc.* **2015**, *137*, 4119−4125.
(29) Bergmann, A.; Martinez-Moreno, E.; Teschner, D.; Chernev, P.; Gliech, M.; de Araujo, J. F.; Reier, T.; Dau, H.; Strasser, P. Reversible Amorphization and the Catalytically Active State of Crystalline Co_3O_4 During Oxygen Evolution. *Nat. Commun.* **2015**, *6*, No. 8625.
(30) Wang, J.; Cui, W.; Liu, Q.; Xing, Z.; Asiri, A. M.; Sun, X. Recent Progress in Cobalt-Based Heterogeneous Catalysts for Electrochemical Water Splitting. *Adv. Mater.* **2016**, *28*, 215−230.
(31) Lado, J. L.; Wang, X.; Paz, E.; Carbó-Argibay, E.; Guldris, N.; Rodríguez-Abreu, C.; Liu, L. F.; Kovnir, K.; Kolen'ko, Y. V. Design and Synthesis of Highly Active Al-Ni-P Foam Electrode for Hydrogen Evolution Reaction. *ACS Catal.* **2015**, *5*, 6503−6508.
(32) Tang, C.; Zhang, R.; Lu, W. B.; He, L. B.; Jiang, X. E.; Asiri, A. M.; Sun, X. P. Fe-Doped CoP Nanoarray: A Monolithic Multifunctional Catalyst for Highly Efficient Hydrogen Generation. *Adv. Mater.* **2017**, *29*, No. 1602441.
(33) Xu, L.; Jiang, Q.; Xiao, Z.; Li, X.; Huo, J.; Wang, S.; Dai, L. Plasma-Engraved Co_3O_4 Nanosheets with Oxygen Vacancies and High Surface Area for the Oxygen Evolution Reaction. *Angew. Chem.* **2016**, *128*, 5363−5367.
(34) Vercesi, G. P.; Rolewicz, J.; Comninellis, C.; Hinder, J. Characterization of dsa-Type Oxygen Evolving Electrodes. Choice of Base Metal. *Thermochim. Acta* **1991**, *176*, 31−47.
(35) Hu, J. M.; Zhang, J. Q.; Meng, H. M.; Zhang, J. Q.; Cao, C. N. Electrochemical Activity, Stability and Degradation Characteristics of IrO_2-Based Electrodes in Aqueous Solutions Containing C_1 Compounds. *Electrochim. Acta* **2005**, *50*, 5370−5378.
(36) Hu, J. M.; Meng, H. M.; Zhang, J. Q.; Cao, C. N. Degradation Mechanism of Long Service Life Ti/IrO_2-Ta_2O_5 Oxide Anodes in Sulphuric Acid. *Corros. Sci.* **2002**, *44*, 1655−1668.
(37) Jiang, J.; Liu, J. P.; Huang, X. T.; Li, Y. Y.; Ding, R. M.; Ji, X. X.; Hu, Y. Y.; Chi, Q. B.; Zhu, Z. H. General Synthesis of Large-Scale Arrays of One-Dimensional Nanostructured Co_3O_4 Directly on Heterogeneous Substrates. *Cryst. Growth Des.* **2010**, *10*, 70−75.
(38) Bandal, H. A.; Jadhav, A. R.; Tamboli, A. H.; Kim, H. Bimetallic Iron Cobalt Oxide Self-Supported on Ni-Foam: An Efficient Bifunctional Electrocatalyst for Oxygen and Hydrogen Evolution Reaction. *Electrochim. Acta* **2017**, *249*, 253−262.
(39) Wang, K.; Shi, Z.; Wang, Y.; Ye, Z.; Xia, H.; Liu, G.; Qiao, G. Co_3O_4 Nanowires@MnO_2 Nanolayer or Nanoflakes Core-Shell Arrays for High-Performance Supercapacitors: the Influence of Morphology on Performance. *J. Alloys Compd.* **2015**, *624*, 85−93.
(40) Zhou, T. T.; Cao, Z.; Wang, H.; Gao, Z.; Li, L.; Ma, H. Y.; Zhao, Y. F. Ultrathin Co-Fe Hydroxide Nanosheet Arrays for Improved Oxygen Evolution During Water Splitting. *RSC Adv.* **2017**, *7*, 22818−22824.
(41) Liu, W.; Liu, H.; Dang, L.; Zhang, H. X.; Wu, X. L.; Yang, B.; Li, Z. J.; Zhang, X. W.; Lei, L. C.; Jin, S. Amorphous Cobalt-Iron Hydroxide Nanosheet Electrocatalyst for Efficient Electrochemical and Photo-Electrochemical Oxygen Evolution. *Adv. Funct. Mater.* **2017**, *27*, No. 1603904.
(42) Giordano, L.; Han, B. H.; Risch, M.; Hong, W. T.; Rao, R. R.; Stoerzinger, K. A.; Shao-Horn, Y. pH Dependence of OER Activity of Oxides: Current and Future Perspectives. *Catal. Today* **2016**, *262*, 2−10.
(43) Rong, X.; Parolin, J.; Kolpak, A. M. A Fundamental Relationship between Reaction Mechanism and Stability in Metal Oxide Catalysts for Oxygen Evolution. *ACS Catal.* **2016**, *6*, 1153−1158.
(44) Seh, Z. W.; Kibsgaard, J.; Dickens, C. F.; Chorkendorff, I.; Nørskov, J. K.; Jaramillo, T. F. Combining Theory and Experiment in Electrocatalysis: Insights into Materials Design. *Science* **2017**, *355*, No. eaad4998.
(45) Anantharaj, S.; Ede, S. R.; Karthick, K.; Sam Sankar, S.; Sangeetha, K.; Karthik, P. E.; Kundu, S. Precision and correctness in the evaluation of electrocatalytic water splitting: revisiting activity parameters with a critical assessment. *Energy Environ. Sci.* **2018**, *11*, 744−771.
(46) Kibsgaard, J.; Chen, Z. B.; Benjamin, N.; Jaramillo, T. F. Engineering the Surface Structure of MoS_2 to Preferentially Expose Active Edge Sites for Electrocatalysis. *Nat. Mater.* **2012**, *11*, 963−969.
(47) Wang, W. G.; Babu, D. D.; Huang, Y. Y.; Lv, J. Q.; Wang, Y. B.; Wu, M. X. Atomic dispersion of Fe/Co/N on graphene by ball-milling for efficient oxygen evolution reaction. *Int. J. Hydrogen Energy* **2018**, *43*, 10351−10358.
(48) Babu, D. D.; Huang, Y. Y.; Anandhababu, G.; Ghausi, M. A.; Wang, Y. B. Mixed-Metal-Organic Framework Self-Template Synthesis of Porous Hybrid Oxyphosphide for Efficient Oxygen Evolution Reaction. *ACS Appl. Mater. Interfaces* **2017**, *9*, 38621−38628.
(49) Wu, X. Z.; Xing, W.; Florek, J.; Zhou, J.; Wang, G. Q.; Zhuo, S. P.; Xue, Q. Z.; Yan, Z. F.; Kleitz, F. On the Origin of the High Capacitance of Carbon Derived from Seaweed with an Apparently Low Surface Area. *J. Mater. Chem. A* **2014**, *2*, 18998−19004.

DOI: 10.1021/acsami.8b15357
ACS Appl. Mater. Interfaces 2018, 10, 39809−39818

(50) Liu, Z.; Tan, X. L.; Gao, X.; Song, L. H. Synthesis of Three-dimensionally Ordered Macroporous Manganese Dioxide-carbon Nanocomposites for Supercapacitors. *J. Power Sources* **2014**, *267*, 812−820.
(51) Ye, Z. G.; Wang, B. F.; Liu, G. W.; Dong, Y. H.; Cui, X.; Peng, X. Y.; Zou, A. H.; Li, D. S. Micropore-Dominant Vanadium and Iron Co-Doped MnO_2 Hybrid Film Electrodes for High-Performance Supercapacitors. *J. Electrochem. Soc.* **2016**, *163*, A2725−A2732.
(52) Hisatomi, T.; Kubota, J.; Domen, K. Recent Advances in Semiconductors for Photocatalytic and Photoelectrochemical Water Splitting. *Chem. Soc. Rev.* **2014**, *43*, 7520−7535.
(53) Liu, Y.; Cai, X. Y.; Luo, B. F.; Yan, M.; Jiang, J. H.; Shi, W. D. MnO_2 Decorated on Carbon Sphere Intercalated Graphene Film for High-performance Supercapacitor Electrodes. *Carbon* **2016**, *107*, 426−432.
(54) Ye, Z. G.; Meng, H. M.; Sun, D. B. New Degradation Mechanism of Ti/IrO_2 + MnO_2 Anode for Oxygen Evolution in 0.5 M H_2SO_4 Solution. *Electrochim. Acta* **2008**, *53*, 5639−5643.
(55) Reier, T.; Oezaslan, M.; Strasser, P. Electrocatalytic Oxygen Evolution Reaction (OER) on Ru, Ir, and Pt Catalysts: A Comparative Study of Nanoparticles and Bulk Materials. *ACS Catal.* **2012**, *2*, 1765−1772.
(56) Lee, Y.; Suntivich, J.; May, K. J.; Perry, E. E.; Shao-Horn, Y. Synthesis and Activities of Rutile IrO_2 and RuO_2 Nanoparticles for Oxygen Evolution in Acid and Alkaline Solutions. *J. Phys. Chem. Lett.* **2012**, *3*, 399−404.
(57) Kötz, R.; Stucki, S. Stabilization of RuO_2 by IrO_2 for Anodic Oxygen Evolution in Acid Media. *Electrochim. Acta* **1986**, *31*, 1311−1316.

DOI: 10.1021/acsami.8b15357
ACS Appl. Mater. Interfaces 2018, 10, 39809−39818